Dative bonding as a mechanism for enhanced catalysis on the surface of MoS_2

Maciej J. Szary[a,*]

[a]*Institute of Physics, Poznan University of Technology, ul. Piotrowo 3, 61-138 Poznan, Poland*

Abstract

Transition-metal dichalcogenide (TMD) layers have been a subject of widespread interest as platforms for electronic devices. However, the low chemical activity of their basal plane results in several technological bottlenecks, including high contact resistance at TMD–electrode interfaces, difficult growth of high-quality gate-oxide layers, and challenging functionalization. The simplest, and perhaps only, approach to overcoming those limitations may be to exploit dative bonding. The effect can enhance binding on TMDs, since their chalcogen nonbonding lone-pair orbitals can function as electron donors. Therefore, it should also be able to impact the surface catalysis for reactions that produce acceptors. This computational study seeks to investigate whether S → P dative bonding may be an effective mechanism for catalysis on the surface of MoS_2, and whether the sheet can be functionalized via chemical reactions enabled by the binding of PH_n and PCl_n. The results show that the bonding facilitates the PH functionalization of MoS_2. The interaction is strong (1.11 eV), making the whole process exothermic, and the activation energy notably reduced (from 2.08 to 0.5 eV). Furthermore, the mechanism is intrinsically selective, which could prove a vital feature for future advancements in TMD-based electronics, since it could steer selected processes toward surface functionalization or thin-film growth.

Keywords: molybdenum disulfide, transition metal dichalcogenides, catalysis, functionalization, surface interactions

1. Introduction

Two-dimensional (2D) transition metal dichalcogenide (TMD) layers are among the most widely studied materials for potential applications in electronic devices [1–8]. The interest stems from the intrinsic properties of TMDs, which arise due to their characteristic structure. Each TMD sheet comprises one transition-metal layer (Mo, W, Pt, etc.) sandwiched between two chalcogen layers (S, Se, Te). The elements within these three layers bond covalently, adopting either trigonal prismatic (1H, 2H for multilayer) or octahedral symmetry (1T), leaving no coordinatively unsaturated surface sites. Consequently, the basal planes of TMD are often chemically inactive, with external interactions limited to van der Waals (vdW) forces. For most TMDs, the sheets can be either semiconducting (1H) or metallic (1T) [9], and for the former, the size of the bandgap depends on the comprising elements and the number of sheets stacked [10–12]. As a result, TMDs offer good chemical stability and a versatile set of electronic properties, which have benefited several high-performance electronic devices, notably chemical sensors and field-effect transistors (FETs). Detectors based on MoS_2 and $MoTe_2$ have been reported as highly sensitive to NO_2 even when operating at room temperature [13–17], despite conventional metal-oxide-semiconductor (MOS) sensors requiring heating to several hundred °C to operate efficiently [18–20]. Likewise, TMD-based FETs have shown improved performance [21–23] and low device-to-device variation [24], illustrating the maturity of the processing technology.

Still, despite the advantages, the intrinsic properties of TMDs have also resulted in several technological bottlenecks. The low chemical activity of the basal plane often results in a high contact resistance at TMD–metal (electrode) interfaces, which can lower the performance of TMD-based electronic devices [25–27]. Furthermore, the lack of unsaturated surface sites hinders the growth of metal oxides on TMD surfaces, despite many applications requiring high-quality gate oxide layers [28–31]. Limited surface interactions also reduce the number of analytes that TMDs can efficiently detect, restricting the application perspectives [32–34]. As a result, significant effort has been put into overcoming those limitations, notably employing substitutional doping [35–39]. The latter has been reported effective in enhancing the local chemical activity of TMDs [40, 41], which has improved the sensitivity of the sheets [42–45] and even facilitated the formation of strong chemical bonds at their surface [46–48]. The doping can be achieved in large-sized single-crystal sheets grown using chemical vapor deposition (CVD) [49–51] and made in pristine sheets employing electron-beam-mediated substitution [52, 53]. Both methods have yielded precise doping levels. However, due to the stochastic nature of the processes, the resulting dopant distribution becomes relatively non-uniform. Hence, despite the reported enhancements, this approach will not be suitable for all applications, especially if a homogeneous functionalization is required. An alternative could be to employ atomic layer deposition (ALD). The technique is well suited to grow high-quality continuous films and has already found extensive use in the fabrication of electronic devices [54–58]. However, the main drawback of ALD use with TMDs is that it often requires coordinatively unsaturated surface sites to initiate the growth process. As a consequence, typical ALD setups have shown only limited success, while optimization approaches employ ultraviolet/O_3 pre-treatment [59, 60], plasma-enhanced ALD [61, 62], or high-temperature annealing [63, 64] to improve nucleation and film quality. Still, regardless of the method, thin and uniform layers grown on TMDs remain a challenge [29, 65].

Given the low reactivity of TMDs, one solution could be to employ reagents that, upon adsorption on the surface of a pristine sheet, would facilitate coordinate covalent (dative) bonding. In most cases, this would imply the use of group III Lewis acids, especially since AlX_3 (X = H, Cl, Br, and CH_3) were predicted to form dative bonds with MoS_2 while in their monomer form [66]. Nevertheless, the compounds are known to dimerize via 3-center 2-electron bonds, and the interaction could prove competitive with the dative bonding due to the conservative binding energy of the latter. Thus, the dimerization could hamper the enhanced adsorption. Furthermore, even if dative bonds form, they were shown to have a limited impact on the molecules. However, with-

*Corresponding author

Email address: maciej.szary@put.poznan.pl (Maciej J. Szary)

out sufficient weakening of the molecular bonds, the activation barriers for subsequent reactions may prove a challenge. Hence, novel solutions are still needed. One such approach could be to find reactions able to functionalize TMD surfaces, since those could be tailored to specific adsorption mechanisms. As a consequence, this study seeks to investigate whether dative bonding may be an effective mechanism for catalysis on the surface of 1H MoS_2, and thus whether the sheet can be functionalized via chemical reactions enabled by the bonding of reduced reaction products.

2. Computational Details

All computations were based on DFT using the projector augmented wave (PAW) method, plane waves (PW), and pseudopotentials (PP), as implemented in the Quantum ESPRESSO suite [67–69]. The employed PPs have included scalar-relativistic and nonlinear core corrections. Due to the slab geometry, the calculations had a dipole correction added to the bare ionic potential [70], and since some of the adsorbates have an uneven number of electrons, all computations were spin unrestricted. The Perdew–Burke–Ernzerhof (PBE) functional [71, 72] was used to approximate the electron exchange-correlation energy, while van der Waals (vdW) contributions to the total energy were treated using Grimme's D3 method [73, 74]. The PBE+D3 treatment has been used since previous reports have shown it to give dative bond energies and distances comparable with those obtained using M06–2X [66, 75] while providing a good description of the electronic properties of TMDs [44, 48]. The PW cutoff energies for the wave function and the electron density were 55 and 450 Ry, respectively. Brillouin-zone integration was performed with a Monkhorst–Pack grid of 6×6×1 [76]. Higher cutoff and larger grids have been tested, and they had little impact on the modeled adsorption. Computations used a Gaussian broadening of 0.001 Ry since the adsorption could result in covalent bonding and thus notably affect the electronics. During total energy optimization, the positions of all atoms were relaxed with the convergence criteria of $<10^{-4}$ Ry/au for the force and $<10^{-5}$ Ry for the total energy. The partial charges were estimated using Löwdin population analysis. Energy barriers were calculated with the nudged elastic band (NEB) method. Atomic schematics given in Figures 1–9 were generated by the XcrySDen program [77].

MoS_2 monolayer was modeled in a 2D periodic slab with a 4×4 supercell and ~ 25 Å of vacuum space between periodically-repeated slabs, which follows the methodology used in other studies of molecular adsorption on MoS_2 [46–48, 66, 78, 79]. In the preliminary stages, the 3×3 and 5×5 structures were also tested, and the results have shown that the 4×4 supercell is a good fit for the investigated problem. In the model system, the adsorption occurs on the upper surface of the sheet, with the lower side remaining pristine. The asymmetry introduces a surface-normal dipole moment resulting from the electron transfer between the sheet and adsorbates, which, given the periodic boundary conditions, gives rise to an artificial electric field between neighboring slabs. Hence, to compensate, a dipole correction layer (DCL) was added in the middle of the vacuum region [70]. Consequently, the width of the vacuum space was set to allow for placement of the DCL such that its half would not overlap with the region above MoS_2, where molecules would adsorb and react with each other.

3. Results and Discussion

3.1. Interactions on surface of MoS_2

The atomic structure of MoS_2 makes the valence of the comprised atoms satisfied. Hence, its surface lacks coordinatively unsaturated sites. This makes the formation of new covalent and ionic bonds typically unfavorable since it would change the chemical bonding structure of the sheet. As a consequence, such interactions are usually exclusive to defected [46–48] or strained TMDs [80] due to the bonding already being affected. It leaves the interactions with the pristine surfaces of MoS_2 mostly limited to vdW forces [79] unless the adsorbate is able to facilitate a dative bond [66].

A dative bond is a two-center, two-electron covalent bond in which both electrons derive from the same atom. In such an interaction, the satisfied valence will make MoS_2 the electron donor, i.e., MoS_2 will share one of its lone electron pairs with an adsorbate acting as the acceptor. Hence, the electron transfer from MoS_2 will most likely involve states at its valence band maximum (VBM). Those states lie at Γ-point for multilayer MoS_2 and K-point for the monolayer. The difference between Γ and K for the latter is relatively low (~ 100 meV). Hence, the charge transfer from MoS_2 could, in principle, originate from the VBM at both Γ and K, depending on the charge density distribution and geometrical constraints. To gain further insight into dative bond formation, the charge-density contours of VBM are shown in Figure 1.

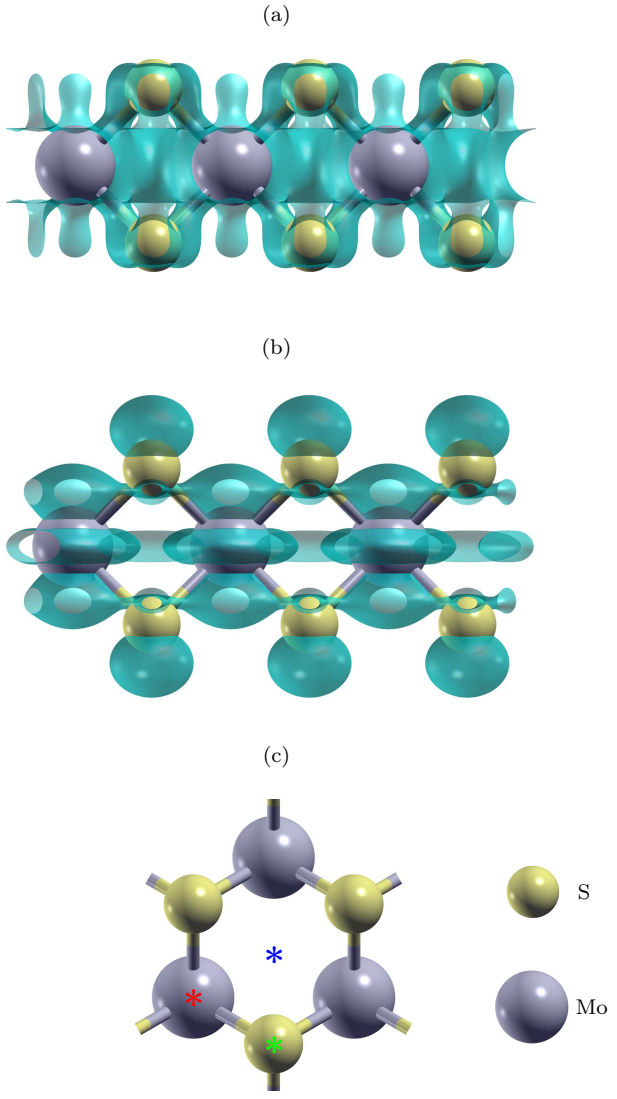

Figure 1: Charge density plots for the VBM of monolayer MoS_2 at (a) Γ-point and (b) K-point of the its (1×1) cell (the isovalue cutoff is 2.5×10^{-3} e/au^{-3}). (c) Adsorption sites on the surface of MoS_2: on-top S, on-top Mo, and hollow.

At K, VBM exhibits a low degree of outward projection since most of the charge is distributed within the sheet (see Figure 1a). It reflects the in-plane character of the comprised orbitals, predominantly $4d_{x^2y^2}$(Mo) and $4d_{xy}$(Mo). In contrast, VBM at Γ has a high contribution of the $3p_z$(S) orbitals, which results in notably more outward charge projection (see Figure 1b). This makes the S nonbonding lone-pair orbital the most readily available electron donor on the surface of MoS_2. Thus, S-site adsorption should be more likely to facilitate dative bonding than other sites like Mo, and hollow (see Figure 1c).

Having the S atoms able to act as an electron donor means that for the dative bond to form, the adsorbate has to be capable of accepting the lone-pair electrons. Such compounds include monomers of Al-bearing Lewis acids (e.g., AlH_3, $AlCl_3$), which have been reported to adsorb on MoS_2 via S → Al dative bond [66]. The mechanism, however, should not be exclusive to group III trichlorides and trihydrides. Rather, dative bonding should be adopted by compounds in which one of its atoms lacks at least two electrons in its valence shell. Therefore, the surface of MoS_2 could prove a suitable catalyst for reactions that produce such compounds. Those could involve group V trichlorides (trihydrides) and hydrogen (chlorine or fluorine) producing hydrogen chloride (HCl) or hydrogen fluoride (HF) since the byproducts would be electron acceptors. Other processes following the same goal could also prove successful. However, they will be beyond the scope of this investigation, which will focus on phosphorus-bearing compounds. The choice has been motivated by the wide use of phosphine (PH_3, see Figure 2a) and phosphorus trichloride (PCl_3, see Figure 2b) in ALD [81–85] and the recent reports showing that phosphorus doping effectively tunes the properties of TMDs [44, 86]. However, other notable advantages of PH_3 and PCl_3 are that they do not dimerize and are easily available.

One of the investigated processes will be a reaction of PH_3 with Cl_2 forming HCl and reduced phosphine. The process will be considered in three stages. At each step, PH_n will dissociate into PH_{n-1} + H, the H atoms will interact with Cl_2 molecules, and HCl will be formed. Each stage will be investigated in gas and on the surface of MoS_2. The former will follow the reactions:

$$2PH_3 + Cl_2 \xrightarrow{\text{Stage 1}} 2PH_2 + 2HCl \quad (1)$$

$$2PH_2 + Cl_2 \xrightarrow{\text{Stage 2}} 2PH + 2HCl \quad (2)$$

$$2PH + Cl_2 \xrightarrow{\text{Stage 3}} 2P + 2HCl \quad (3)$$

which can be summarized as

$$2PH_3 + 3Cl_2 \xrightarrow{\text{Stage 1, 2, 3}} 2P + 6HCl \quad (4)$$

The latter will follow equivalent reactions, but on MoS_2, so to differentiate the two, the processes will be denoted as:

$$2PH_3@MoS_2 + 3Cl_2 \xrightarrow{\text{Stage 1, 2, 3}} 2P@MoS_2 + 6HCl \quad (5)$$

The second of the investigated processes will be a reaction of PH_3 with F_2. In this case, three similar stages will also be considered, but rather than forming HCl, they will produce HF, which will make the reaction more energetically favorable than the previous one. Each stage will be investigated in gas and on the surface of MoS_2, following total formulas:

$$2PH_3 + 3F_2 \xrightarrow{\text{Stage 1, 2, 3}} 2P + 6HF \quad (6)$$

$$2PH_3@MoS_2 + 3F_2 \xrightarrow{\text{Stage 1, 2, 3}} 2P@MoS_2 + 6HF \quad (7)$$

The third process will involve PCl_3 and H_2. Similar to the first reaction, this one will also produce HCl, but the byproduct will be reduced phosphorous chloride. The process will be considered in three stages. At each step, PCl_n will dissociate into PCl_{n-1} + Cl, and the Cl atoms will interact with H_2, which will form HCl. Again, each stage will be investigated in gas and on the surface of MoS_2.

$$2PCl_3 + 3H_2 \xrightarrow{\text{Stage 1, 2, 3}} 2P + 6HCl \quad (8)$$

$$2PCl_3@MoS_2 + 3H_2 \xrightarrow{\text{Stage 1, 2, 3}} 2P@MoS_2 + 6HCl \quad (9)$$

The last process will involve PCl_3 and H_2O. Again, HCl will be formed. However, the P-bearing molecule will not dissociate like in previous cases. Rather, one of the Cl atoms will be substituted by the OH group, i.e., $PCl_n(OH)_m + H_2O \rightarrow PCl_{n-1}(OH)_{m+1} + HCl$. As a consequence, the reaction will not produce an electron acceptor, which means that the products will not facilitate dative bonding with S atoms of MoS_2. On the other hand, the product will be a less favorable tautomer to phosphorous acid (H_3PO_3), which should be an optimal case for enhanced interactions other than coordinate bonding. Hence, the inclusion of this process serves to illustrate how reactive is the surface in the case where the dative bonding is not the leading mechanism of the surface interactions. The process will be investigated in three stages, and each stage will be considered in gas and on the surface of MoS_2, following two formulas:

$$PCl_3 + 3H_2O \xrightarrow{\text{Stage 1, 2, 3}} P(OH)_3 + 3HCl \quad (10)$$

$$PCl_3@MoS_2 + 3H_2O \xrightarrow{\text{Stage 1, 2, 3}} P(OH)_3@MoS_2 + 3HCl \quad (11)$$

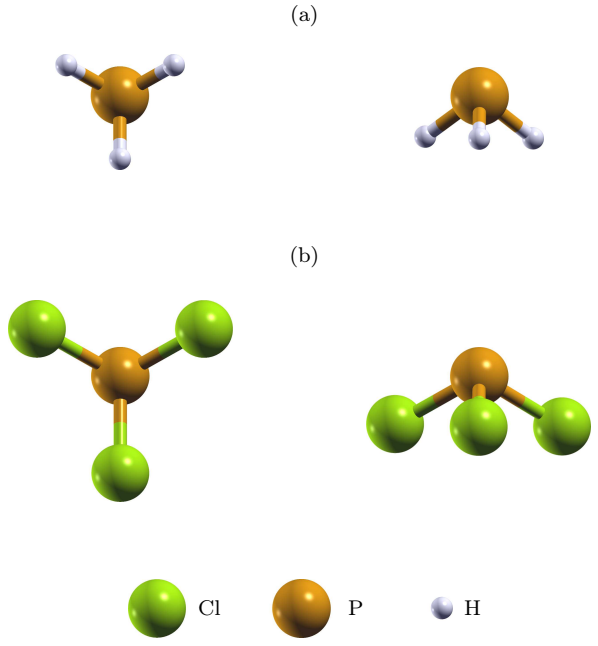

Figure 2: Atomic structures of (a) PH_3 and (b) PCl_3.

3.2. Adsorption of PH_3 and PCl_3 on surface of MoS_2

Prior to the chemical reactions described in Section 3.1, the adsorption of PH_3 and PCl_3 will be most likely governed by a combination of vdW and electrostatic effects. Thus, the adsorption will not favor one well-defined site but will result in several different configurations characterized by similar adsorption energies and separated by low energy barriers. As a consequence, MoS_2 will not impose a predefined geometry for the reagents to interact. Hence, several distinct configurations should be considered and used for different reaction geometries. Both molecules are a trigonal pyramid (see Figures 2a and 2b), which makes their adsorption describable with two parameters, namely, (i) the position of the side atoms, and (ii) whether the phosphorus is facing towards or away from the surface. In principle, the former could be random. However, due to the hexagonal symmetry of MoS_2, the problem can be reduced to just two rotary configurations. Together this gives four distinct configurations for each molecule to probe the S-site adsorption, i.e., D1 (Figure 3a), D2 (Figure 3b), U1 (Figure 3c), and U2 (Figure 3d). In addition, D1 adsorption will be investigated for Mo and hollow sites (Figures 3e and 3f). The sites are unlikely to facilitate a dative bond. Hence, their inclusion should illustrate the impact of the dative bond on the total energy, and/or if the molecules can spontaneously shift towards more favorable sites during the reactions.

Table 1 summarizes the adsorption of PH_3 and PCl_3 on MoS_2. The parameters include the molecule bond distances ($d_{H–P}$ and $d_{Cl–P}$), the vertical separation between the molecule and the surface (h_{mol}), and the adsorption energy (E_{ads}). The latter is defined as

$$E_{ads} = E(PX_3@MoS_2) - E(PX_3) - E(MoS_2), \qquad (12)$$

where $E(PX_3@MoS_2)$, $E(PX_3)$, and $E(MoS_2)$ are the total energy of the adsorbate-substrate system, free molecule (PH_3 or PCl_3), and the monolayer, respectively. Thus, E_{ads} is positive for endothermic and negative for exothermic processes. The optimized structures of the most and least favorable configurations are shown in Figure 4, while the remaining geometries are included in Supporting Information (see Figures S1 and S2).

The results show that the adsorption of PH_3 and PCl_3 shares qualitative similarities for both molecules. In all investigated cases, the adsorption is an exothermic process. The values of E_{ads} are relatively low, indicating weak surface interactions. This coincides with the large vertical separation between the molecules and MoS_2, which far exceeds the sum of the covalent radii of the interfacing atoms. Furthermore, the molecules themselves show virtually no change upon adsorption or differences between configurations. Those features are characteristic of the adsorption, where interactions are limited to a combination of vdW and electrostatic effects. Due to their dispersive nature, the positions of the side atoms have a negligible effect on the value of E_{ads}. On the

Table 1: Adsorption of PH_3 and PCl_3 on monolayer MoS_2

Mol.	Site	Config.	Fig.	$-E_{ads}$ [a]	$d_{H/Cl–P}$ [b]	h_{mol} [c]
PH_3	S	D1	4b	115	1.431	3.809
		D2	S1e	115	1.430	3.811
		U1	4a	174	1.431	3.014
		U2	S1f	172	1.431	3.025
	Mo	D1	S1b	169	1.431	3.237
	hollow	D1	S1a	156	1.431	3.340
PCl_3	S	D1	4d	236	2.076	3.501
		D2	S2e	237	2.075	3.496
		U1	S2d	360	2.075	3.307
		U2	S2f	356	2.075	3.294
	Mo	D1	4c	375	2.079	2.798
	hollow	D1	S2a	325	2.075	3.019

[a] E_{ads} is the adsortion energy (eq X, given in meV), [b] $d_{H–P}$ and $d_{Cl–P}$ are the bond distances in the molecules of PH_3 and PCl_3, respectively (given in Å), [c] h_{mol} is the vertical separation between the molecule and MoS_2 (given in Å).

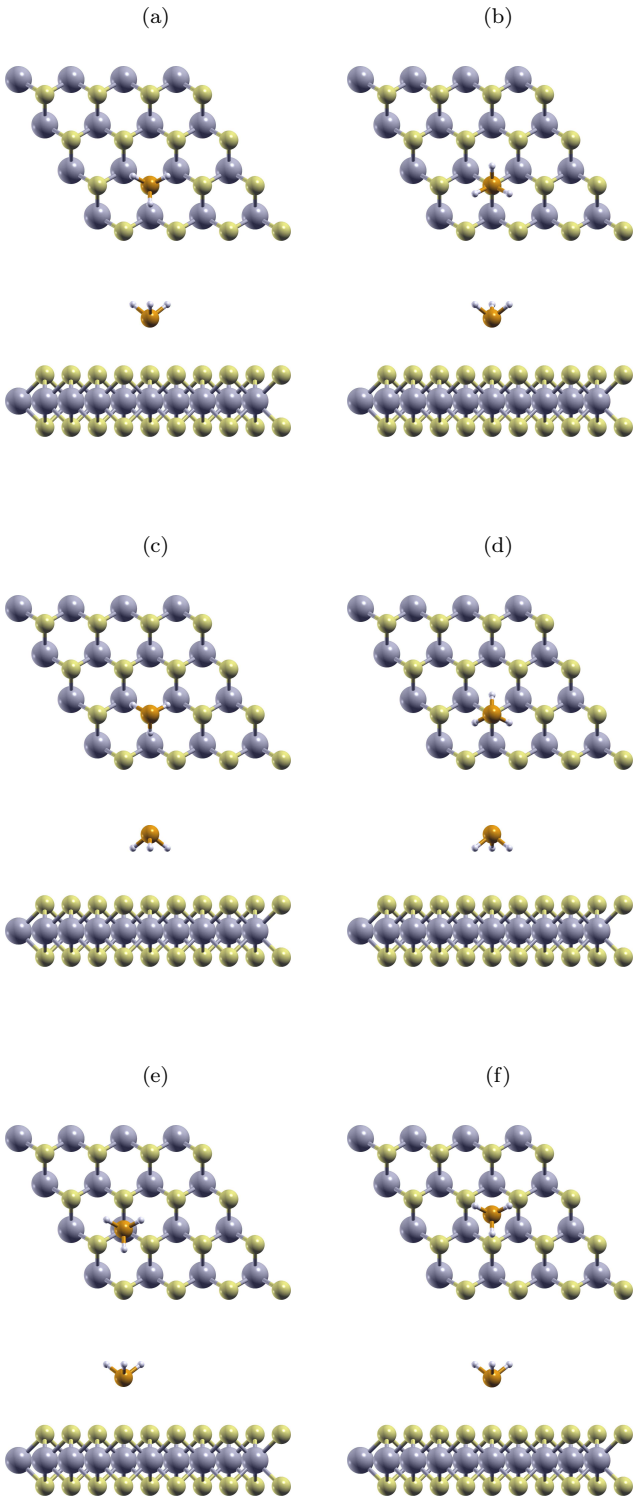

Figure 3: Schematics of initial adsorption geometries (a) D1, (b) D2, (c) U1, and (d) U2 at the S-site. D1 configurations at (e) Mo- and (f) hollow-sites. In the case of PCl_3, the configurations are equivalent.

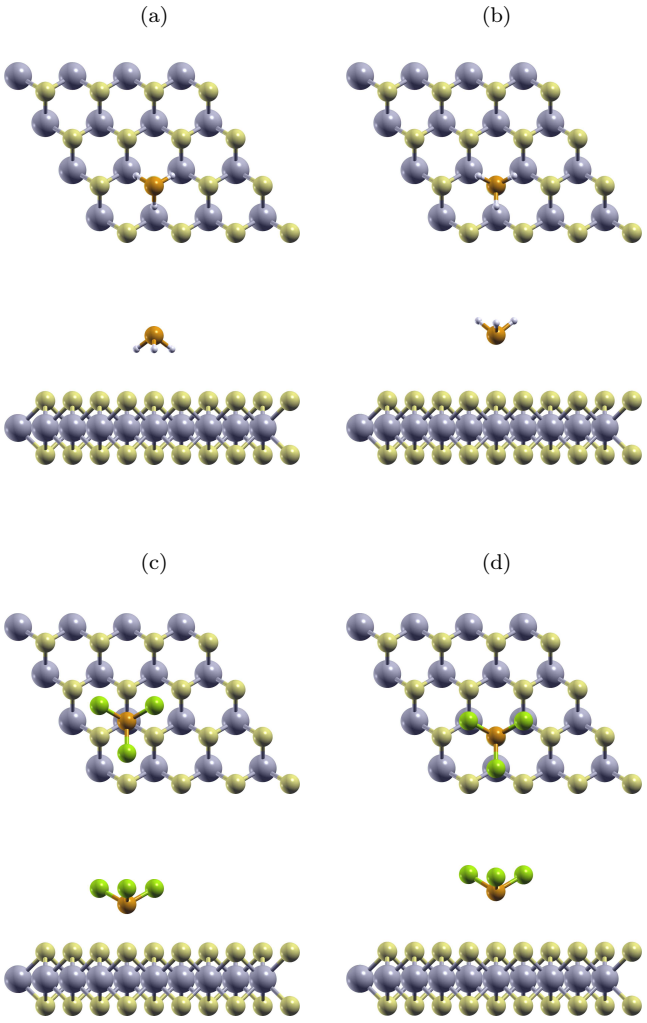

Figure 4: The optimized atomic structures of most (a) and least (b) favorable configuration of PH_3@MoS_2. The optimized atomic structures of most (c) and least (d) favorable configuration of PCl_3@MoS_2.

other hand, adsorption sites and the position of phosphorus show some impact on the adsorption energy. However, at room temperature, these differences should not have a significant effect on the adsorption.

It is also prudent to note that the results show that, regardless of the adsorption geometry, PCl_3 has higher absorption energy than PH_3. The minimum and maximum values of E_{ads} for PCl_3 are −236 and −375 meV, while E_{ads} for PH_3 ranges between −115 and −173 meV. The difference is notable. However, it has nothing to do with the dative bonding. The effect is to be expected, since PCl_3 has a greater dipole moment (0.97 D) than PH_3 (0.58 D). The PCl_3-to-PH_3 ratio of the average E_{ads} (2.19) is comparable to the ratio of the dipole moments of the molecules (2.02), which suggests that vdW forces are the dominant component of the interaction.

3.3. Reactions of PH_3 and PCl_3

Phosphorus has a valence of 3 in both PH_3 and PCl_3. This satisfies the electronic pairs on its valence shell, which means that the molecules will act as electron donors rather than acceptors. Hence, to make them acceptors, a reaction has to reduce the valence. However, this requires the molecules to dissociate, $PX_n \rightarrow PX_{n-1} + X$, which on its own is endothermic, but, at least in principle, could be offset by the exothermic formation energy of the other reaction products and the formation of S → P dative bond, making the reaction favorable. Furthermore, since each dissociation will impact the molecular bonds, some stages may prove more favorable than others, and thus each should be investigated to elucidate the total energy of the reaction (E_{rxn}) and the molecule-sheet interactions (i.e., E_{ads}). The latter will be best illustrated by the difference between the reaction energies occurring on MoS_2 and in gas

$$E_{ads} = E_{rxn}(@MoS_2) - E_{rxn}(gas), \tag{13}$$

where each E_{rxn} will differ for each reaction. In the case of the Cl_2 + PH_3, the reaction energy in gas will follow the formula

$$E_{rxn} = E(PH_{3-n}) + nE(HCl) - E(PH_3) - \frac{n}{2}E(Cl_2), \tag{14}$$

where E is the total energy, and n is the stage of the reaction ($n = 0, 1, 2, 3$). Consequently, E_{rxn} of Cl_2 + PH_3 reacting on MoS_2 will be calculated as

$$\begin{aligned} E_{rxn} = {} & E(PH_{3-n}@MoS_2) + nE(HCl) \\ & - E(PH_3) - E(@MoS_2) - \frac{n}{2}E(Cl_2). \end{aligned} \tag{15}$$

Therefore, E_{rxn} represents the total energy of the products relative to the energy of non-interacting reagents. By analogy, the reaction energy for F_2 + PH_3 occurring in gas and on MoS_2 will follow formulas

$$E_{rxn} = E(PH_{3-n}) + nE(HF) - E(PH_3) - \frac{n}{2}E(F_2), \tag{16}$$

$$\begin{aligned} E_{rxn} = {} & E(PH_{3-n}@MoS_2) + nE(HF) \\ & - E(PH_3) - E(@MoS_2) - \frac{n}{2}E(F_2). \end{aligned} \tag{17}$$

Finally, the values of E_{rxn} for the last dissociative reaction H_2 + PCl_3 will be calculated using formulas

$$E_{rxn} = E(PCl_{3-n}) + nE(HCl) - E(PCl_3) - \frac{n}{2}E(H_2), \tag{18}$$

$$\begin{aligned} E_{rxn} = {} & E(PCl_{3-n}@MoS_2) + nE(HCl) \\ & - E(PCl_3) - E(@MoS_2) - \frac{n}{2}E(H_2). \end{aligned} \tag{19}$$

$E(PX_{3-n})$ and $E(PX_{3-n}@MoS_2)$ are calculated in such a way that, for each step of the reaction, one X atom of the P-bearing molecule is removed from the system, and then the structure is optimized to give a new total energy. Subsequently, the new geometry becomes the starting point for the next step, and the process continues up to $n = 3$ (i.e., the bare phosphorus).

Figure 5a shows the values of E_{rxn} for Cl_2 + PH_3 (stage "0" indicates the pre-reaction state of the system). In the gas phase, steps 1–3 have E_{rxn} of 0.48, 0.75, and 2.56 eV, respectively. The trend is not linear, indicating that PH_{3-n} species reconfigure their molecular bonds, which affects the subsequent dissociation energies. The positive values of the reaction energy show that the process is endothermic, meaning that the exothermic formation of HCl is not enough to offset the dissociation, and thus for this reaction to be favorable, the difference would have to be compensated by enhanced molecule-sheet interactions of the byproducts.

In the case of Cl_2 + PH_3@MoS_2, there is no one geometry for the reagents to interact. Hence, the three-step procedure has been repeated for all adsorption configurations discussed in Section 3.2. Still, despite the differences in the initial position of PH_3, all computations have converged on the qualitatively same geometries and thus are equivalent for stages 1–3. For stage 0, Figure 5a shows E_{rxn} of the highest- (empty circle, dashed line) and the lowest-energy configurations (full circle, solid

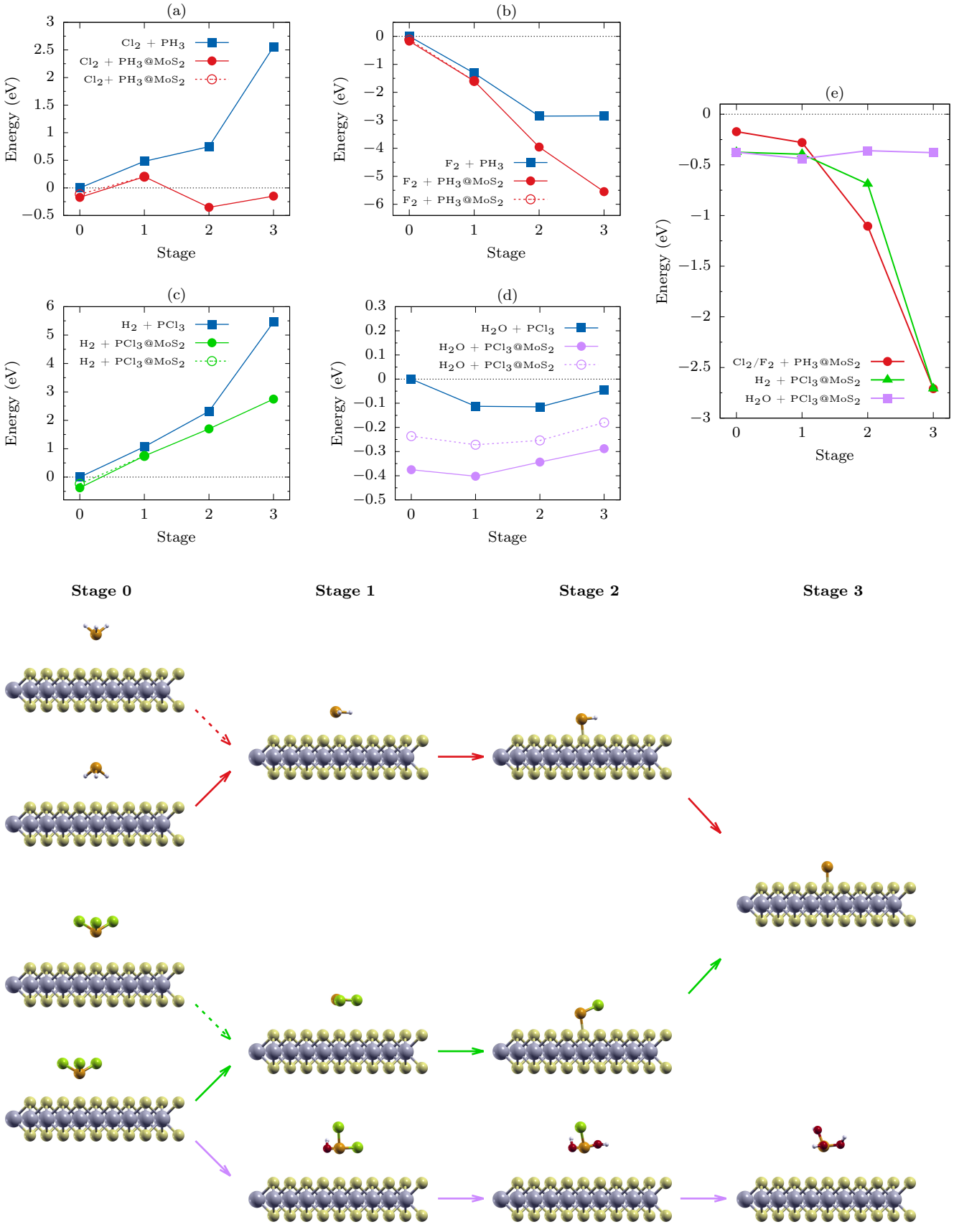

Figure 5: (a–d) The energies of the reactions at each step of the process. For the @MoS_2 configurations only the values for the most and least favorable configurations are shown. (e) The adsorption energies of the phosphorus-bearing products. Bottom half of the figure includes the diagram illustrating the structures at each stage of the reaction, arrow types coincide with the line styles used in the graphs a–e.

line). Both structures are also included in the diagram in Figure 5, where the dashed arrow leads from the highest-energy configuration, while the solid one leads from the lowest. In stage 1, the loss of the H atom causes PH_2 to favor a geometry where the molecule orients itself "flat" centered at the nearest-neighbor S-site (see stage 1 graphic in Figure 5). The molecule binds more strongly to the surface. However, the effect is limited ($E_{ads} > -0.17$ eV for PH_3 vs. $E_{ads} \approx -0.28$ eV for PH_2, see Figure 5e) and thus cannot be a result of dative bonding. More likely, this is a product of a weak bonding interaction between the unpaired electron of phosphorus and the lone pair of sulfur, since it would account for the small increase of E_{ads} and the reduced, but still relatively large, distances between the atoms (> 3.5 Å for PH_3 vs. ≈ 2.8 Å for PH_2). As a consequence, the change in binding energy is insufficient to compensate for the dissociation or compete with the adsorption. Thus, the first stage on MoS_2 is slightly endothermic ($E_{rxn} = 0.2$ eV) but more favorable than reacting in the gas phase. In stage 2, PH_2 dissociates into PH and H, which has a notable impact on the molecule-sheet interactions. PH retains the in-plain configuration, but the phosphorous shifts towards the nearest sulfur atom (see stage 2 in Figure 5). The resulting S–P distance is only 2.069 Å, which is within the sum of the covalent radii of both atoms. This coincides with a charge transfer from $3p_z$(S) orbital to $3p$(P) and a significant increase of adsorption energy ($E_{ads} = -1.11$ eV, see Figure 5e). In contrast, the sheet of MoS_2 remains unaffected. Hence, the only mechanism that could account for the effect is an S → P dative bonding. The interaction becomes favorable since the phosphorus in PH lacks two electrons to satisfy its valence, making the molecule an electron acceptor and thus allowing a donation of lone-pair electrons. The strong binding reduces the reaction energy to −0.35 eV, making stage 2 exothermic and favorable over simple adsorption of PH_3. This illustrates that dative bonding on the surface of MoS_2 can enable the catalysis of a reaction, which otherwise is endothermic. Finally, in stage 3 the last H − P bond breaks, leaving a bare phosphorus. It increases the adsorption energy of P even further ($E_{ads} = -2.71$ eV, see Figure 5e). However, since the last dissociation is the most endothermic, the resulting E_{rxn} is only −0.15 eV (see Figure 5a). As a consequence, the third remains exothermic, but it is less favorable than the second stage. Hence, the PH functionalization of MoS_2 remains the lowest energy configuration of the system.

Figure 5b shows the values of E_{rxn} for F_2+PH_3 and F_2+PH_3@MoS_2. In contrast to the previous reaction, $F_2 + PH_3$ is predicted energetically favorable, with stages 1–3 having E_{rxn} of −1.32, −2.85, and −2.84 eV, respectively. The results indicate that a dative bond is not required to enable the dissociation of PH_3, and that the reaction should be able to initiate without MoS_2. However, this should not be confused with the surface having a negligible impact on the process. The low reaction energy of $F_2 + PH_3$ stems from the exothermic formation of HF. It offsets the endothermic dissociation of F_2 and PH_3 in stage 1, continues in stage 2 with the dissociation of F_2 and PH_2, but ends at stage 3, where formation energy of HF is only able to equal the exothermic dissociation of F_2 and PH (stages 2 and 3 have virtually identical E_{rxn}, see Figure 5b). This means that HF formation is not a sufficient mechanism to facilitate stage 3. Thus, other exothermic effects are required. The results show that one of those could be dative bonding on MoS_2. Figure 5b illustrates that each stage of $F_2 + PH_3$@MoS_2 has a lower value of E_{rxn} than $F_2 + PH_3$. The difference for subsequent steps becomes more pronounced due to the enhanced adsorption of the P-bearing compounds (see Figure 5e). This makes each step of F_2 + PH_3@MoS_2 more favorable than the previous. Therefore, improving the catalysis for processes on MoS_2.

Figure 5c gives E_{rxn} for H_2+PCl_3 and H_2+PCl_3@MoS_2. In contrast to both previous processes, the reaction is not energetically favorable. In gas, the reaction energies for stages 1–3 are 1.07, 2.32, and 5.46 eV, respectively. The values indicate that the formation of HCl is insufficient to offset the dissociation of H_2 and PCl_3. On MoS_2, the difference is reduced by the molecule-sheet interactions, but the reaction energy remains positive. In stage 1, the loss of the Cl atom causes all initial configurations to favor a geometry where PCl_2 orients itself in-plane, centered at the nearest-neighbor S-site, as was the case for PH_2 (see stage 1 graphic in Figure 5). The dissociation has a limited impact on the adsorption energy ($E_{ads} = -0.4$ eV, see Figure 5e). However, this changes in stage 2. Here, PCl aligns itself flat with the phosphorous above the nearest sulfur atom (see stage 2 in Figure 5). It results in an S–P distance of 2.114 Å and an E_{ads} of −0.69 eV. The S → P bond energy for PCl@MoS_2 is comparable to S → Al for AlH_3@MoS_2 (−0.7 eV) and $AlCl_3$@MoS_2 (−0.79 eV) [66]. However, all three are notably weaker than S → P for PH@MoS_2 (−1.11 eV), suggesting that less electronic charge available on the molecule demands a stronger dative bonding. Finally, at stage 3, both PH_3@MoS_2 and PCl_3@MoS_2 processes converge on the same structure, giving rise to strong binding of the phosphorous atom ($E_{ads} = -2.71$ eV). Still, the effect is not enough to compensate for the dissociation of PCl_3. Hence, all stages remain endothermic, which shows that a process can be unfavorable even if dative bonds can form.

The results discussed so far have covered only reactions that facilitate dative bonding. Hence, it is prudent to contrast the findings with a process where the mechanism is unavailable, i.e., $H_2O + PCl_3$. In this case, the P-bearing molecule will not dissociate, but Cl atoms will be substituted by OH groups, as denoted by formulas (10) and (11). The reaction will not produce electron acceptors, and thus dative bonds will not be formed. The values of E_{rnx} for the substitution will be calculated using formulas

$$E_{rxn} = E[PCl_{3-n}(OH)_n] + nE(HCl) - E(PCl_3) - nE(H_2O), \quad (20)$$

$$E_{rxn} = E[PCl_{3-n}(OH)_n@MoS_2] + nE(HCl) - E(PCl_3@MoS_2) - nE(H_2O), \quad (21)$$

where E is the total energy, and n is the stage of the reaction. Figure 5d shows the values of E_{rxn} for $H_2O + PCl_3$ and $H_2O + PCl_3$@MoS_2. For the reactions on MoS_2, only the values for the most and least favorable configurations are shown. The atomic structures of the former are also given at the bottom of the diagram in Figure 5. The results show that in gas, the reaction is slightly exothermic, which corresponds with the molecule being a tautomer of H_3PO_3. However, even in their less stable forms, the products do not facilitate improved binding with the surface of MoS_2. The adsorption has no significant effect on the molecular bonds, the molecule-sheet distances are high (> 3.3 Å), and the binding is weak, all indicating that the adsorption is governed by vdW forces. However, due to the dispersive nature of the interactions, the adsorption energy shows little change despite the substitution (see Figure 5e), which means that MoS_2 will not catalyze the reaction.

The investigated processes illustrate that MoS_2 can affect the reaction energy. However, the effect can vary notably. It depends on whether the reaction facilitates the formation of dative bonds, which in turn requires products that are electron acceptors. Without them, surface interactions remain governed by vdW forces. Thus, making the impact of MoS_2 negligible. As a consequence, the effect is not available to all reactions, and thus it cannot be employed universally for enhanced surface catalysis on MoS_2. Nevertheless, this could also prove an advantage, since the intrinsic selectivity of the mechanism may steer some processes toward surface functionalization and/or thin-film growth. The effectiveness would depend on the competing paths, but if the functionalization was an exothermic reaction, and the corresponding activation energy would be sufficiently low, dative bonding could make the process dominant.

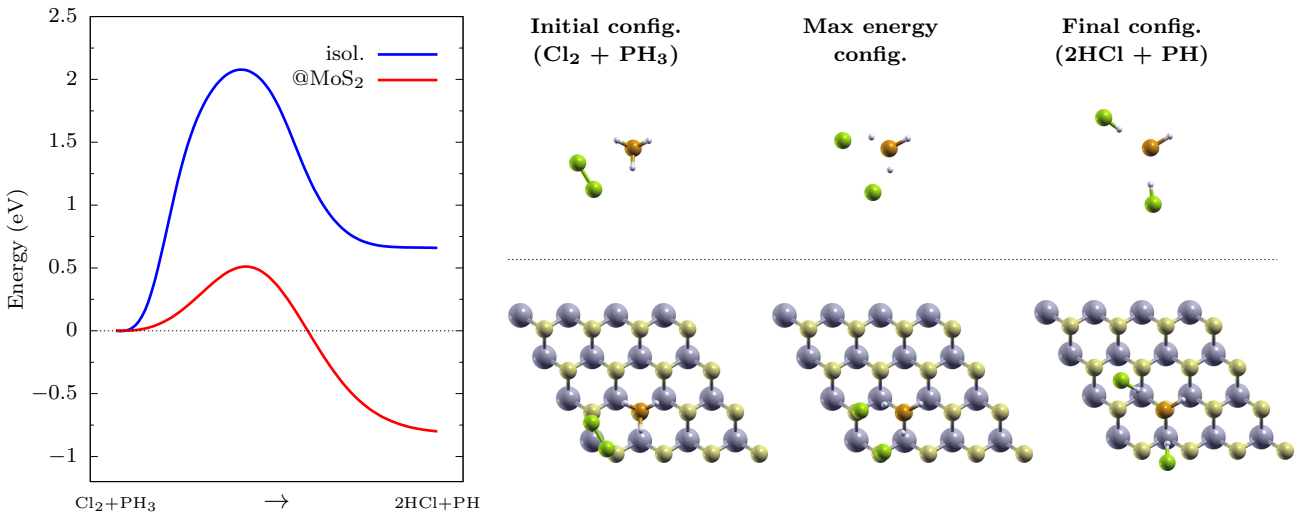

Figure 6: NEB paths calculated for (blue) $Cl_2 + PH_3 \rightarrow 2HCl + PH$ and (red) $Cl_2 + PH_3@MoS_2 \rightarrow 2HCl + PH@MoS_2$.

$Cl_2 + PH_3@MoS_2$ is predicted endothermic in stage 1 and exothermic for stages 2 and 3. This suggests that the most likely scenario for the process is going directly from stage 0 to stage 2, i.e., a case where one Cl_2 reacts with one PH_3 forming two HCl and one PH. Figure 6 shows the energy barriers of the reaction in gas and on MoS_2. The former represents an endothermic process. However, it is included for the purpose of comparison. The results show that the surface has a notable effect on both the final energy and the corresponding barrier. In gas, the activation energy is 2.08 eV, while on MoS_2, this is reduced to just 0.5 eV. The difference coincides with the shift in final energy, which indicates the dominant role of the S → P dative bond even at the early stages of the process. The role of the molecule-sheet binding is further illustrated by the reaction paths. In both cases, the processes adopt equivalent configurations, and thus the only difference that could significantly affect the barrier height is the S → P bond. It is also important to note that the lower values of the final energy relative to the values given in Figure 5a result from HCl adsorption on MoS_2. The latter is not included in the E_{rnx} to focus only on the exothermic impact of dative bonding. Together, the results suggest that MoS_2 could have a notable impact on the formation of HCl. However, this still depends on the competing reactions. In this case, the most likely alternative would be a process where Cl substitutes H and H_2 is formed as it would produce a precursor to PCl_5.

Figure7 shows total energy as a function of reaction coordinates for $Cl_2 + PH_3 \rightarrow H_2 + PHCl_2$ and $Cl_2 + PH_3@MoS_2 \rightarrow 2HCl + PH@MoS_2$. The results show that both reactions are exothermic but have notably different energies. The formation of Cl − P bonds in $PHCl_2$ results in a lower reaction energy (−1.61 eV) than the formation of PH on MoS_2 (−0.8 eV). However, the former has a significantly higher barrier of 1.78 eV, resulting from the dissociation of PH_3 and Cl_2 (see the maximum energy configuration in Figure 7). On the other hand, the S → P bond enables the low barrier of 0.5 eV for the latter. Hence, due to the low activation energy, the functionalization on MoS_2 should be a faster reaction outside of the high-temperature, high-pressure limit, whereas, within it, the H-to-Cl substitution should become dominant due to the lower total energy.

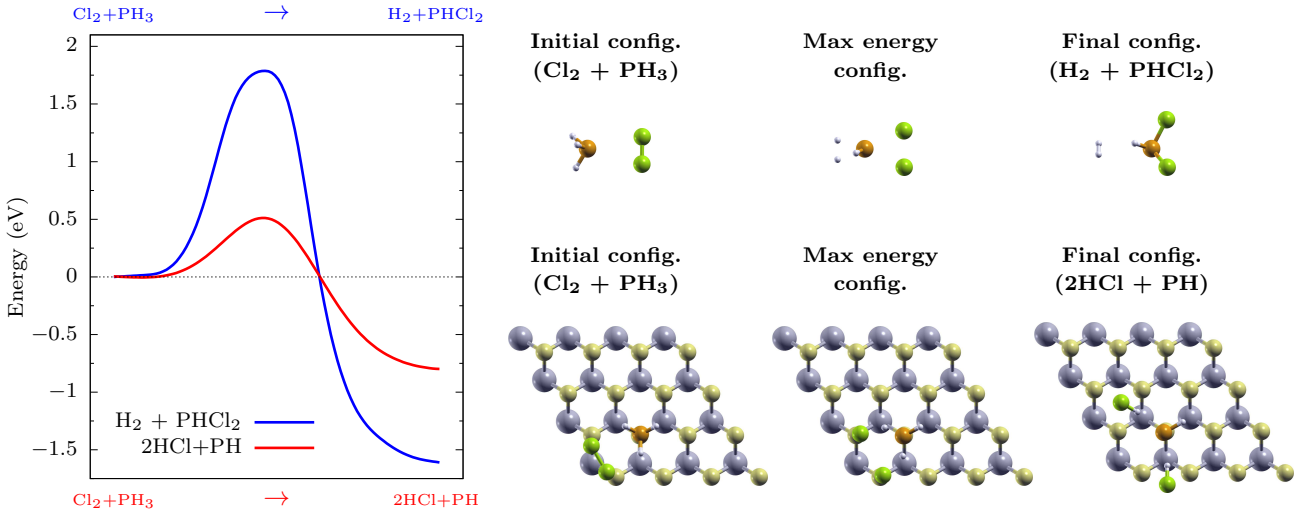

Figure 7: NEB paths calculated for (blue) $Cl_2 + PH_3 \rightarrow H_2 + PHCl_2$ and (red) $Cl_2 + PH_3@MoS_2 \rightarrow 2HCl + PH@MoS_2$.

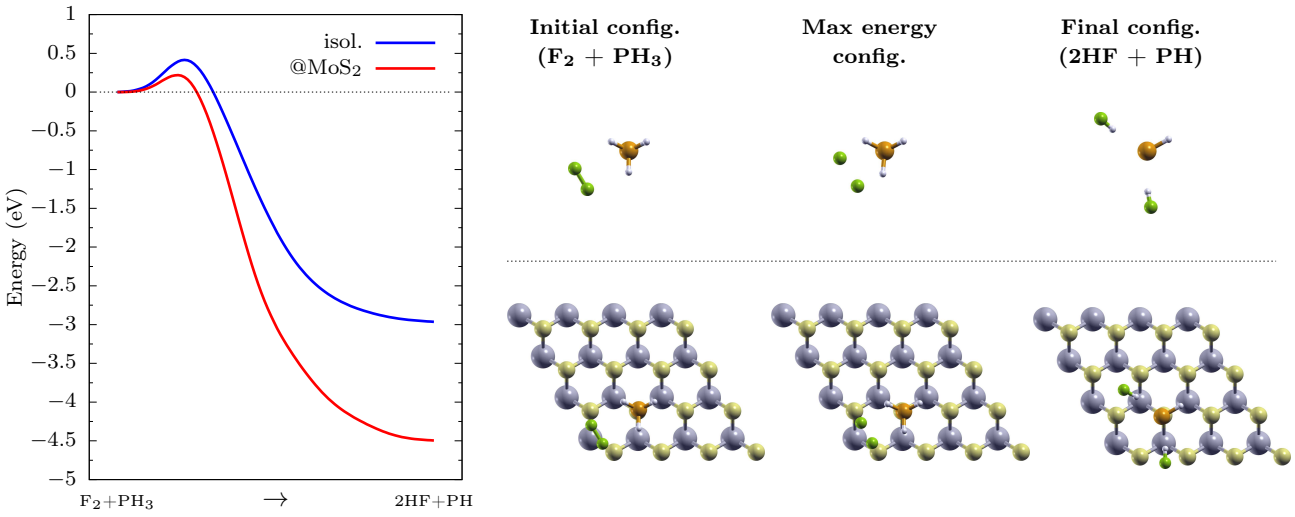

Figure 8: NEB paths calculated for (blue) $F_2 + PH_3 \rightarrow 2HF + PH$ and (red) $F_2 + PH_3@MoS_2 \rightarrow 2HF + PH@MoS_2$.

In the case of F_2+PH_3, HF formation will most likely be a dominant reaction, resulting from the strong binding between H and F, and the relatively weak bonds of P and F. Thus, the effectiveness of HF formation will mostly depend on the activation energy. Figure 8 shows total energy as a function of reaction coordinates for $F_2 + PH_3 \rightarrow 2HF + PH$ occurring in the gas phase and on the surface of MoS_2. The results illustrate that MoS_2 has a considerable impact on the final energy but a limited effect on the height of the energy barrier. The low value of the final energy is facilitated by the S → P bonding and the physisorption of HF, similar to the effects described for $Cl_2 + PH_3$. However, unlike the reaction with chlorine, the dative bonding is not formed immediately alongside the dissociation of fluorine. F – F bonds are weaker than the Cl – Cl, and thus at the early stages of the reaction, F_2 breaks first with only some bending of H – P bonds in PH_3 (see the maximum energy structures in Figure 8). This means that there are no available electron acceptors, since PH is not fully formed. Consequently, the impact of MoS_2 on the barrier height is limited, shifting the value by −0.27 eV. Even so, the difference is still relevant because the original value is low (0.41 eV). As a consequence, the barrier on MoS_2 is only 0.16 eV, which means that the reaction could be considerably faster on the surface.

Considering that the results predict a few routes for PH functionalization of MoS_2, it remains prudent to investigate whether surface diffusion of adsorbed species is possible. The lowest energy path for PH diffusion between two nearest-neighbor S-sites is shown in Figure 9. The NEB computations give the PH path with P moving linearly between the sites and H moving alongside. The path has two maxima (configurations "a" and "c" in Figure 9) and a local minimum right between the S-sites (configuration "b"). The results give the total activation energy of ≈ 0.8 eV. This suggests that the diffusion is possible as the value

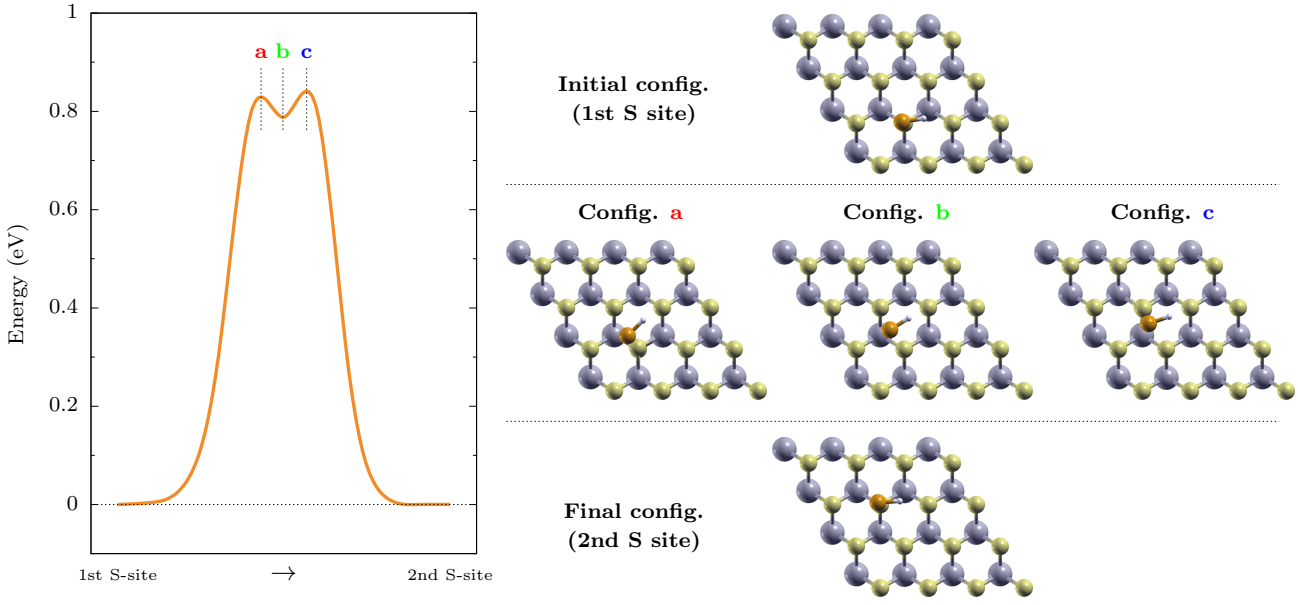

Figure 9: NEB paths calculated for PH diffusion between nearest-neighbor S-sites.

is sufficiently lower that the PH desperation energy of 1.11 eV. However, since the barrier is still high, the process will be slow and limited to high temperatures. Thus, the metastable configuration will have a neglectable impact on the diffusion as it is separated by small energy barriers of only ≈ 20 meV.

4. Conclusions

The present work demonstrates a computational investigation of the functionalization of MoS_2 via chemical reactions that facilitate dative bonds between the products and the MoS_2 substrate. To achieve that the investigation employs the dissociation of phosphine and phosphorus trichloride. The results show that the reduced valence of the phosphorus enables the donation of electrons from $3p_z$(S) orbitals to $3p$(P) in an S → P dative bond. The predicted binding is strong and shown to occur for all initial configurations. It enables the interaction to affect the catalysis, but the effectiveness depends on the reaction.

The mechanism seems to be the most successful in combination with moderately endothermic processes like HCl and PH_n formation from Cl_2 and PH_3. In gas, the reaction is predicted endothermic. However, dative bonding makes the process exothermic, favoring the PH functionalization of MoS_2. The interaction also significantly lowers the activation energy (from 2.08 to 0.5 eV), which could make the reaction dominant in the mid-temperature limit, since processes like PCl_5 formation require much higher activation (1.78 eV). Dative bonding can also improve the catalysis for more energetically favorable reactions, e.g., F_2 and PH_3 producing HF and PH_n, acting as another exothermic component. Thus, compensating for the endothermic dissociation and lowering the total energy. However, for highly exothermic processes, e.g., H_2 and PCl_3 forming HCl and PCl_n, S → P is insufficient to compensate for the dissociation, and thus the mechanism is unable to facilitate such reaction on the surface of MoS_2.

Finally, the results show a stark contrast to reactions where dative bonding is unavailable, i.e., H_2O and PCl_3 forming HCl and $P(OH)_3$. Here, the interactions with the adsorbates are limited to weak vdW and electrostatic effects, which results in MoS_2 having virtually no effect on the catalysis of the reaction. The results illustrate that dative bonding is crucial for enhancing catalysis on MoS_2. However, this requires products that are electron acceptors. Thus, the effect is not available to all reactions. Nevertheless, the intrinsic selectivity of the mechanism could prove an advantage, since it can steer selected processes toward surface functionalization and/or thin-film growth. Therefore, the mechanism could prove vital for future advancements in TMD-based electronics.

Acknowledgments

This work was supported by the Ministry of Education and Science in Poland (Grant No. 0512/SBAD/2320) within the project realized at the Institute of Physics, Poznan University of Technology. Computations reported in this work have been performed at Poznan Supercomputing and Networking Center (PSNC) under Grant No. 608.

References

[1] T. Liu, D. Xiang, Y. Zheng, Y. Wang, X. Wang, L. Wang, J. He, L. Liu, W. Chen, Nonvolatile and programmable photodoping in $MoTe_2$ for photoresist-free complementary electronic devices, Advanced Materials 30 (52) (2018) 1804470. arXiv:https://onlinelibrary.wiley.com/doi/pdf/10.1002/adma.201804470, doi:https://doi.org/10.1002/adma.201804470.
URL https://onlinelibrary.wiley.com/doi/abs/10.1002/adma.201804470

[2] L. Wang, L. Chen, S. L. Wong, X. Huang, W. Liao, C. Zhu, Y.-F. Lim, D. Li, X. Liu, D. Chi, K.-W. Ang, Electronic devices and circuits based on wafer-scale polycrystalline monolayer MoS_2 by chemical vapor deposition, Advanced Electronic Materials 5 (8) (2019) 1900393. arXiv:https://onlinelibrary.wiley.com/doi/pdf/10.1002/aelm.201900393, doi:https://doi.org/10.1002/aelm.201900393.
URL https://onlinelibrary.wiley.com/doi/abs/10.1002/aelm.201900393

[3] E. Singh, P. Singh, K. S. Kim, G. Y. Yeom, H. S. Nalwa, Flexible molybdenum disulfide (MoS_2) atomic layers for wearable electronics and optoelectronics, ACS Applied Materials & Interfaces 11 (12) (2019) 11061–11105. arXiv:https://doi.org/10.1021/acsami.8b19859, doi:10.1021/acsami.8b19859.
URL https://doi.org/10.1021/acsami.8b19859

[4] Q. Cheng, J. Pang, D. Sun, J. Wang, S. Zhang, F. Liu, Y. Chen, R. Yang, N. Liang, X. Lu, Y. Ji, J. Wang, C. Zhang, Y. Sang, H. Liu, W. Zhou, WSe_2 2D p-type semiconductor-based electronic devices for information technology: Design, preparation, and applications, InfoMat 2 (4) (2020) 656–697. arXiv:https://onlinelibrary.wiley.com/doi/pdf/10.1002/inf2.12093, doi:https://doi.org/10.1002/inf2.12093.
URL https://onlinelibrary.wiley.com/doi/abs/10.1002/inf2.12093

[5] R. Kumar, N. Goel, M. Hojamberdiev, M. Kumar, Transition metal dichalcogenides-based flexible gas sensors, Sensors and Actuators A: Physical 303 (2020) 111875. doi:https://doi.org/10.1016/j.sna.2020.111875.
URL https://www.sciencedirect.com/science/article/pii/S092442471931903X

[6] M. S. Vidhya, R. Yuvakkumar, G. Ravi, B. Saravanakumar, D. Velauthapillai, Asymmetric polyhedron structured $NiSe_2$@$MoSe_2$ device for use as a supercapacitor, Nanoscale Adv. 3 (2021) 4207–4215. doi:10.1039/D0NA01047B.
URL http://dx.doi.org/10.1039/D0NA01047B

[7] Y. Jeong, H. J. Lee, J. Park, S. Lee, H.-J. Jin, S. Park, H. Cho, S. Hong, T. Kim, K. Kim, S. Choi, S. Im, Engineering $MoSe_2$/MoS_2 heterojunction traps in 2d transistors for multilevel memory, multiscale display, and synaptic functions, npj 2D Materials and Applications 6 (1) (2022) 23. doi:10.1038/s41699-022-00295-8.
URL https://doi.org/10.1038/s41699-022-00295-8

[8] R. Kaur, K. Singh, S. Tripathi, Electrical, linear and non-linear optical properties of $MoSe_2$/PVA nanocomposites as charge trapping elements for memory device applications, Journal of Alloys and Compounds 905 (2022) 164103. doi:https://doi.org/10.1016/j.jallcom.2022.164103.
URL https://www.sciencedirect.com/science/article/pii/S0925838822004947

[9] Q. H. Wang, K. Kalantar-Zadeh, A. Kis, J. N. Coleman, M. S. Strano, Electronics and optoelectronics of two-dimensional transition metal dichalcogenides, Nature Nanotechnology 7 (11) (2012) 699–712. doi:10.1038/nnano.2012.193.
URL https://doi.org/10.1038/nnano.2012.193

[10] J. Gusakova, X. Wang, L. L. Shiau, A. Krivosheeva, V. Shaposhnikov, V. Borisenko, V. Gusakov, B. K. Tay, Electronic properties of bulk and monolayer TMDs: Theoretical study within DFT framework (GVJ-2e method), physica status solidi (a) 214 (12) (2017) 1700218. arXiv:https://onlinelibrary.wiley.com/doi/pdf/10.1002/pssa.201700218, doi:https://doi.org/10.1002/pssa.201700218.
URL https://onlinelibrary.wiley.com/doi/abs/10.1002/pssa.201700218

[11] M. Kang, B. Kim, S. H. Ryu, S. W. Jung, J. Kim, L. Moreschini, C. Jozwiak, E. Rotenberg, A. Bostwick, K. S. Kim, Universal mechanism of band-gap engineering in transition-metal dichalcogenides, Nano Letters 17 (3) (2017) 1610–1615, pMID: 28118710. arXiv:https://doi.org/10.1021/acs.nanolett.6b04775, doi:10.1021/acs.nanolett.6b04775.
URL https://doi.org/10.1021/acs.nanolett.6b04775

[12] A. Chaves, J. G. Azadani, H. Alsalman, D. R. da Costa, R. Frisenda, A. J. Chaves, S. H. Song, Y. D. Kim, D. He, J. Zhou, A. Castellanos-Gomez,

F. M. Peeters, Z. Liu, C. L. Hinkle, S.-H. Oh, P. D. Ye, S. J. Koester, Y. H. Lee, P. Avouris, X. Wang, T. Low, Bandgap engineering of two-dimensional semiconductor materials, npj 2D Materials and Applications 4 (1) (2020) 29. doi:10.1038/s41699-020-00162-4.
URL https://doi.org/10.1038/s41699-020-00162-4

[13] Z. Feng, Y. Xie, J. Chen, Y. Yu, S. Zheng, R. Zhang, Q. Li, X. Chen, C. Sun, H. Zhang, W. Pang, J. Liu, D. Zhang, Highly sensitive $MoTe_2$ chemical sensor with fast recovery rate through gate biasing, 2D Materials 4 (2) (2017) 025018. doi:10.1088/2053-1583/aa57fe.
URL https://dx.doi.org/10.1088/2053-1583/aa57fe

[14] E. Wu, Y. Xie, B. Yuan, H. Zhang, X. Hu, J. Liu, D. Zhang, Ultrasensitive and fully reversible NO_2 gas sensing based on p-type $MoTe_2$ under ultraviolet illumination, ACS Sensors 3 (9) (2018) 1719–1726, pMID: 30105902. arXiv:https://doi.org/10.1021/acssensors.8b00461, doi:10.1021/acssensors.8b00461.
URL https://doi.org/10.1021/acssensors.8b00461

[15] M. Reddeppa, B.-G. Park, G. Murali, S. H. Choi, N. D. Chinh, D. Kim, W. Yang, M.-D. Kim, NO_2 gas sensors based on layer-transferred n-MoS_2/p-GaN heterojunction at room temperature: Study of UV light illuminations and humidity, Sensors and Actuators B: Chemical 308 (2020) 127700. doi:https://doi.org/10.1016/j.snb.2020.127700.
URL https://www.sciencedirect.com/science/article/pii/S0925400520300472

[16] W. Zheng, Y. Xu, L. Zheng, C. Yang, N. Pinna, X. Liu, J. Zhang, MoS_2 van der waals p–n junctions enabling highly selective room-temperature NO_2 sensor, Advanced Functional Materials 30 (19) (2020) 2000435. arXiv:https://onlinelibrary.wiley.com/doi/pdf/10.1002/adfm.202000435, doi:https://doi.org/10.1002/adfm.202000435.
URL https://onlinelibrary.wiley.com/doi/abs/10.1002/adfm.202000435

[17] C. Liu, X. Chen, H. Luo, B. Li, J. Shi, C. Fan, J. Yang, M. Zeng, Z. Zhou, N. Hu, Y. Su, Z. Yang, Highly sensitive and recoverable room-temperature NO_2 gas detection realized by 2D/0D MoS_2/ZnS heterostructures with synergistic effects, Sensors and Actuators B: Chemical 347 (2021) 130608. doi:https://doi.org/10.1016/j.snb.2021.130608.
URL https://www.sciencedirect.com/science/article/pii/S092540052101176X

[18] J. Chang, H. Kuo, I. Leu, M. Hon, The effects of thickness and operation temperature on ZnO:Al thin film CO gas sensor, Sensors and Actuators B: Chemical 84 (2) (2002) 258–264. doi:https://doi.org/10.1016/S0925-4005(02)00034-5.
URL https://www.sciencedirect.com/science/article/pii/S0925400502000345

[19] R. Binions, A. Naik, 13 - metal oxide semiconductor gas sensors in environmental monitoring, in: R. Jaaniso, O. K. Tan (Eds.), Semiconductor Gas Sensors, Woodhead Publishing Series in Electronic and Optical Materials, Woodhead Publishing, 2013, pp. 433–466. doi:https://doi.org/10.1533/9780857098665.4.433.
URL https://www.sciencedirect.com/science/article/pii/B9780857092366500137

[20] S. Navale, V. Jadhav, K. Tehare, R. Sagar, C. Biswas, M. Galluzzi, W. Liang, V. Patil, R. Mane, F. Stadler, Solid-state synthesis strategy of ZnO nanoparticles for the rapid detection of hazardous Cl_2, Sensors and Actuators B: Chemical 238 (2017) 1102–1110. doi:https://doi.org/10.1016/j.snb.2016.07.136.
URL https://www.sciencedirect.com/science/article/pii/S0925400516311807

[21] A. Nourbakhsh, A. Zubair, R. N. Sajjad, A. Tavakkoli K. G., W. Chen, S. Fang, X. Ling, J. Kong, M. S. Dresselhaus, E. Kaxiras, K. K. Berggren, D. Antoniadis, T. Palacios, MoS_2 field-effect transistor with sub-10 nm channel length, Nano Letters 16 (12) (2016) 7798–7806, pMID: 27960446. arXiv:https://doi.org/10.1021/acs.nanolett.6b03999, doi:10.1021/acs.nanolett.6b03999.
URL https://doi.org/10.1021/acs.nanolett.6b03999

[22] D. Seo, D. Y. Lee, J. Kwon, J. J. Lee, T. Taniguchi, K. Watanabe, G.-H. Lee, K. S. Kim, J. Hone, Y. D. Kim, H.-J. Choi, High-performance monolayer MoS_2 field-effect transistor with large-scale nitrogen-doped graphene electrodes for Ohmic contact, Applied Physics Letters 115 (1) (2019) 012104. arXiv:https://doi.org/10.1063/1.5094682, doi:10.1063/1.5094682.
URL https://doi.org/10.1063/1.5094682

[23] L. Tao, Y. Zhou, J.-B. Xu, Phase-controlled epitaxial growth of $MoTe_2$: Approaching high-quality 2D materials for electronic devices with low contact resistance, Journal of Applied Physics 131 (11) (2022) 110902. arXiv:https://doi.org/10.1063/5.0073650, doi:10.1063/5.0073650.
URL https://doi.org/10.1063/5.0073650

[24] A. Sebastian, R. Pendurthi, T. H. Choudhury, J. M. Redwing, S. Das, Benchmarking monolayer MoS_2 and WS_2 field-effect transistors, Nature Communications 12 (1) (2021) 693. doi:10.1038/s41467-020-20732-w.
URL https://doi.org/10.1038/s41467-020-20732-w

[25] H.-Y. Chang, W. Zhu, D. Akinwande, On the mobility and contact resistance evaluation for transistors based on MoS_2 or two-dimensional semiconducting atomic crystals, Applied Physics Letters 104 (11) (2014) 113504. arXiv:https://doi.org/10.1063/1.4868536, doi:10.1063/1.4868536.
URL https://doi.org/10.1063/1.4868536

[26] N. Kaushik, D. Karmakar, A. Nipane, S. Karande, S. Lodha, Interfacial n-doping using an ultrathin TiO_2 layer for contact resistance reduction in MoS_2, ACS Applied Materials & Interfaces 8 (1) (2016) 256–263, pMID: 26649572. arXiv:https://doi.org/10.1021/acsami.5b08559, doi:10.1021/acsami.5b08559.
URL https://doi.org/10.1021/acsami.5b08559

[27] J. Jang, Y. Kim, S.-S. Chee, H. Kim, D. Whang, G.-H. Kim, S. J. Yun, Clean interface contact using a zno interlayer for low-contact-resistance MoS_2 transistors, ACS Applied Materials & Interfaces 12 (4) (2020) 5031–5039, pMID: 31891246. arXiv:https://doi.org/10.1021/acsami.9b18591, doi:10.1021/acsami.9b18591.
URL https://doi.org/10.1021/acsami.9b18591

[28] S. McDonnell, B. Brennan, A. Azcatl, N. Lu, H. Dong, C. Buie, J. Kim, C. L. Hinkle, M. J. Kim, R. M. Wallace, HfO_2 on $MoSe_2$ by atomic layer deposition: Adsorption mechanisms and thickness scalability, ACS Nano 7 (11) (2013) 10354–10361, pMID: 24116949. arXiv:https://doi.org/10.1021/nn404775u, doi:10.1021/nn404775u.
URL https://doi.org/10.1021/nn404775u

[29] H. Zhang, D. Chiappe, J. Meersschaut, T. Conard, A. Franquet, T. Nuytten, M. Mannarino, I. Radu, W. Vandervorst, A. Delabie, Nucleation and growth mechanisms of Al_2O_3 atomic layer deposition on synthetic polycrystalline MoS_2, The Journal of Chemical Physics 146 (5) (2017) 052810. arXiv:https://doi.org/10.1063/1.4967406, doi:10.1063/1.4967406.
URL https://doi.org/10.1063/1.4967406

[30] T. Nam, S. Seo, H. Kim, Atomic layer deposition of a uniform thin film on two-dimensional transition metal dichalcogenides, Journal of Vacuum Science & Technology A 38 (3) (2020) 030803. arXiv:https://doi.org/10.1116/6.0000068, doi:10.1116/6.0000068.
URL https://doi.org/10.1116/6.0000068

[31] L. Zhang, H. Xing, M. Yang, Q. Dong, H. Li, S. Liu, Advances in atomic layer deposited high-κ inorganic materials for gate dielectrics engineering of two-dimensional MoS_2 field effect transistors, Carbon Letters 32 (5) (2022) 1247–1264. doi:10.1007/s42823-022-00367-1.
URL https://doi.org/10.1007/s42823-022-00367-1

[32] Q. Yue, Z. Shao, S. Chang, J. Li, Adsorption of gas molecules on monolayer MoS_2 and effect of applied electric field, Nanoscale Research Letters 8 (1) (2013) 425. doi:10.1186/1556-276X-8-425.
URL https://doi.org/10.1186/1556-276X-8-425

[33] S. Zhao, J. Xue, W. Kang, Gas adsorption on MoS_2 monolayer from first-principles calculations, Chemical Physics Letters 595-596 (2014) 35–42. doi:https://doi.org/10.1016/j.cplett.2014.01.043.
URL https://www.sciencedirect.com/science/article/pii/S0009261414000529

[34] A. Abbasi, J. J. Sardroodi, Adsorption of O_3, SO_2 and SO_3 gas molecules on MoS_2 monolayers: A computational investigation, Applied Surface Science 469 (2019) 781–791. doi:https://doi.org/10.1016/j.apsusc.2018.11.039.
URL https://www.sciencedirect.com/science/article/pii/S0169433218331076

[35] H.-J. Chuang, B. Chamlagain, M. Koehler, M. M. Perera, J. Yan, D. Mandrus, D. Tománek, Z. Zhou, Low-resistance 2D/2D Ohmic contacts: A universal approach to high-performance WSe_2, MoS_2, and $MoSe_2$ transistors, Nano Letters 16 (3) (2016) 1896–1902, pMID: 26844954.

arXiv:https://doi.org/10.1021/acs.nanolett.5b05066, doi:10.1021/acs.nanolett.5b05066.
URL https://doi.org/10.1021/acs.nanolett.5b05066

[36] T. Kim, Y. Kim, E. K. Kim, Characteristics of Cl-doped MoS_2 field-effect transistors, Sensors and Actuators A: Physical 312 (2020) 112165. doi:https://doi.org/10.1016/j.sna.2020.112165.
URL https://www.sciencedirect.com/science/article/pii/S0924424720300881

[37] F. Zhong, J. Ye, T. He, L. Zhang, Z. Wang, Q. Li, B. Han, P. Wang, P. Wu, Y. Yu, J. Guo, Z. Zhang, M. Peng, T. Xu, X. Ge, Y. Wang, H. Wang, M. Zubair, X. Zhou, P. Gao, Z. Fan, W. Hu, Substitutionally doped $MoSe_2$ for high-performance electronics and optoelectronics, Small 17 (47) (2021) 2102855. arXiv:https://onlinelibrary.wiley.com/doi/pdf/10.1002/smll.202102855, doi:https://doi.org/10.1002/smll.202102855.
URL https://onlinelibrary.wiley.com/doi/abs/10.1002/smll.202102855

[38] Z. Wei, J. Tang, X. Li, Z. Chi, Y. Wang, Q. Wang, B. Han, N. Li, B. Huang, J. Li, H. Yu, J. Yuan, H. Chen, J. Sun, L. Chen, K. Wu, P. Gao, C. He, W. Yang, D. Shi, R. Yang, G. Zhang, Wafer-scale oxygen-doped MoS_2 monolayer, Small Methods 5 (6) (2021) 2100091. arXiv:https://onlinelibrary.wiley.com/doi/pdf/10.1002/smtd.202100091, doi:https://doi.org/10.1002/smtd.202100091.
URL https://onlinelibrary.wiley.com/doi/abs/10.1002/smtd.202100091

[39] H. Li, M. Cheng, P. Wang, R. Du, L. Song, J. He, J. Shi, Reducing contact resistance and boosting device performance of monolayer MoS_2 by in situ Fe doping, Advanced Materials 34 (18) (2022) 2200885. arXiv:https://onlinelibrary.wiley.com/doi/pdf/10.1002/adma.202200885, doi:https://doi.org/10.1002/adma.202200885.
URL https://onlinelibrary.wiley.com/doi/abs/10.1002/adma.202200885

[40] Y.-C. Lin, D. O. Dumcenco, H.-P. Komsa, Y. Niimi, A. V. Krasheninnikov, Y.-S. Huang, K. Suenaga, Properties of individual dopant atoms in single-layer MoS_2: Atomic structure, migration, and enhanced reactivity, Advanced Materials 26 (18) (2014) 2857–2861. arXiv:https://onlinelibrary.wiley.com/doi/pdf/10.1002/adma.201304985, doi:https://doi.org/10.1002/adma.201304985.
URL https://onlinelibrary.wiley.com/doi/abs/10.1002/adma.201304985

[41] M. J. Szary, J. A. Babelek, D. M. Florjan, Dopant-sheet interaction and its role in the enhanced chemical activity of doped $MoTe_2$, Surface Science 723 (2022) 122093. doi:https://doi.org/10.1016/j.susc.2022.122093.
URL https://www.sciencedirect.com/science/article/pii/S0039602822000784

[42] P. Panigrahi, T. Hussain, A. Karton, R. Ahuja, Elemental substitution of two-dimensional transition metal dichalcogenides ($MoSe_2$ and $MoTe_2$): Implications for enhanced gas sensing, ACS Sensors 4 (10) (2019) 2646–2653, pMID: 31565924. arXiv:https://doi.org/10.1021/acssensors.9b01044, doi:10.1021/acssensors.9b01044.
URL https://doi.org/10.1021/acssensors.9b01044

[43] D. Burman, H. Raha, B. Manna, P. Pramanik, P. K. Guha, Substitutional doping of MoS_2 for superior gas-sensing applications: A proof of concept, ACS Sensors 6 (9) (2021) 3398–3408, pMID: 34494827. arXiv:https://doi.org/10.1021/acssensors.1c01258, doi:10.1021/acssensors.1c01258.
URL https://doi.org/10.1021/acssensors.1c01258

[44] M. J. Szary, D. M. Florjan, J. A. Babelek, Selective detection of carbon monoxide on p-block doped monolayers of $MoTe_2$, ACS Sensors 7 (1) (2022) 272–285, pMID: 35044171. arXiv:https://doi.org/10.1021/acssensors.1c02246, doi:10.1021/acssensors.1c02246.
URL https://doi.org/10.1021/acssensors.1c02246

[45] S. G. Ramaraj, S. Nundy, P. Zhao, D. Elamaran, A. A. Tahir, Y. Hayakawa, M. Muruganathan, H. Mizuta, S.-W. Kim, RF sputtered Nb-doped MoS_2 thin film for effective detection of NO_2 gas molecules: Theoretical and experimental studies, ACS Omega 7 (12) (2022) 10492–10501. arXiv:https://doi.org/10.1021/acsomega.1c07274, doi:10.1021/acsomega.1c07274.
URL https://doi.org/10.1021/acsomega.1c07274

[46] X. Deng, X. Liang, S.-P. Ng, C.-M. L. Wu, Adsorption of formaldehyde on transition metal doped monolayer MoS_2: A DFT study, Applied Surface Science 484 (2019) 1244–1252. doi:https://doi.org/10.1016/j.apsusc.2019.04.175.
URL https://www.sciencedirect.com/science/article/pii/S0169433219311869

[47] M. J. Szary, J. A. Bąbelek, D. M. Florjan, Adsorption and dissociation of NO_2 on MoS_2 doped with p-block elements, Surface Science 712 (2021) 121893. doi:https://doi.org/10.1016/j.susc.2021.121893.
URL https://www.sciencedirect.com/science/article/pii/S0039602821000972

[48] M. J. Szary, Adsorption of ethylene oxide on doped monolayers of MoS_2: A DFT study, Materials Science and Engineering: B 265 (2021) 115009. doi:https://doi.org/10.1016/j.mseb.2020.115009.
URL https://www.sciencedirect.com/science/article/pii/S092151072030516X

[49] Y. Yang, J. Shang, H. Gao, Q. Sun, L. Kou, Z.-G. Chen, J. Zou, Intercalation-induced disintegrated layer-by-layer growth of ultrathin ternary $Mo(Te_{1-x}S_x)_2$ plates, ACS Applied Materials & Interfaces 12 (27) (2020) 30980–30989, pMID: 32515585. arXiv:https://doi.org/10.1021/acsami.0c07342, doi:10.1021/acsami.0c07342.
URL https://doi.org/10.1021/acsami.0c07342

[50] S.-S. Chee, H. Jang, K. Lee, M.-H. Ham, Substitutional fluorine doping of large-area molybdenum disulfide monolayer films for flexible inverter device arrays, ACS Applied Materials & Interfaces 12 (28) (2020) 31804–31809, pMID: 32559366. arXiv:https://doi.org/10.1021/acsami.0c07824, doi:10.1021/acsami.0c07824.
URL https://doi.org/10.1021/acsami.0c07824

[51] W. Li, J. Huang, B. Han, C. Xie, X. Huang, K. Tian, Y. Zeng, Z. Zhao, P. Gao, Y. Zhang, T. Yang, Z. Zhang, S. Sun, Y. Hou, Molten-salt-assisted chemical vapor deposition process for substitutional doping of monolayer MoS_2 and effectively altering the electronic structure and phononic properties, Advanced Science 7 (16) (2020) 2001080. arXiv:https://onlinelibrary.wiley.com/doi/pdf/10.1002/advs.202001080, doi:https://doi.org/10.1002/advs.202001080.
URL https://onlinelibrary.wiley.com/doi/abs/10.1002/advs.202001080

[52] H.-P. Komsa, J. Kotakoski, S. Kurasch, O. Lehtinen, U. Kaiser, A. V. Krasheninnikov, Two-dimensional transition metal dichalcogenides under electron irradiation: Defect production and doping, Phys. Rev. Lett. 109 (2012) 035503. doi:10.1103/PhysRevLett.109.035503.
URL https://link.aps.org/doi/10.1103/PhysRevLett.109.035503

[53] H.-P. Komsa, S. Kurasch, O. Lehtinen, U. Kaiser, A. V. Krasheninnikov, From point to extended defects in two-dimensional MoS_2: Evolution of atomic structure under electron irradiation, Phys. Rev. B 88 (2013) 035301. doi:10.1103/PhysRevB.88.035301.
URL https://link.aps.org/doi/10.1103/PhysRevB.88.035301

[54] D. H. Levy, S. F. Nelson, D. Freeman, Oxide electronics by spatial atomic layer deposition, Journal of Display Technology 5 (12) (2009) 484–494. doi:10.1109/JDT.2009.2022770.

[55] D. H. Levy, S. F. Nelson, Thin-film electronics by atomic layer deposition, Journal of Vacuum Science & Technology A 30 (1) (2012) 018501. arXiv:https://doi.org/10.1116/1.3670748, doi:10.1116/1.3670748.
URL https://doi.org/10.1116/1.3670748

[56] W. L. I. Waduge, Y. Chen, P. Zuo, N. Jayakodiarachchi, T. F. Kuech, S. E. Babcock, P. G. Evans, C. H. Winter, Solid-phase epitaxy of perovskite high dielectric $PrAlO_3$ films grown by atomic layer deposition for use in two-dimensional electronics and memory devices, ACS Applied Nano Materials 2 (11) (2019) 7449–7458. arXiv:https://doi.org/10.1021/acsanm.9b02153, doi:10.1021/acsanm.9b02153.
URL https://doi.org/10.1021/acsanm.9b02153

[57] J. W. Maina, A. Merenda, M. Weber, J. M. Pringle, M. Bechelany, L. Hyde, L. F. Dumée, Atomic layer deposition of transition metal films and nanostructures for electronic and catalytic applications, Critical Reviews in Solid State and Materials Sciences 46 (5) (2021) 468–489. arXiv:https://doi.org/10.1080/10408436.2020.1819200, doi:10.1080/10408436.2020.1819200.
URL https://doi.org/10.1080/10408436.2020.1819200

[58] T. Ciuk, L. Ciura, P. Michałowski, J. Jagiełło, A. Dobrowolski, K. Piętak, D. Kalita, M. Wzorek, R. Budzich, D. Czołak, A. Kolek,

Contamination-induced inhomogeneity of noise sources distribution in Al_2O_3-passivated quasi-free-standing graphene on 4H-SiC(0001), Physica E: Low-dimensional Systems and Nanostructures 142 (2022) 115264. doi:https://doi.org/10.1016/j.physe.2022.115264.
URL https://www.sciencedirect.com/science/article/pii/S1386947722001126

[59] A. Azcatl, S. KC, X. Peng, N. Lu, S. McDonnell, X. Qin, F. de Dios, R. Addou, J. Kim, M. J. Kim, K. Cho, R. M. Wallace, HfO_2 on UV-O_3 exposed transition metal dichalcogenides: interfacial reactions study, 2D Materials 2 (1) (2015) 014004. doi:10.1088/2053-1583/2/1/014004.
URL https://dx.doi.org/10.1088/2053-1583/2/1/014004

[60] S. Park, S. Y. Kim, Y. Choi, M. Kim, H. Shin, J. Kim, W. Choi, Interface properties of atomic-layer-deposited Al_2O_3 thin films on ultraviolet/ozone-treated multilayer MoS_2 crystals, ACS Applied Materials & Interfaces 8 (18) (2016) 11189–11193, pMID: 27117229. arXiv:https://doi.org/10.1021/acsami.6b01568, doi:10.1021/acsami.6b01568.
URL https://doi.org/10.1021/acsami.6b01568

[61] K. M. Price, K. E. Schauble, F. A. McGuire, D. B. Farmer, A. D. Franklin, Uniform growth of sub-5-nanometer high-κ dielectrics on MoS_2 using plasma-enhanced atomic layer deposition, ACS Applied Materials & Interfaces 9 (27) (2017) 23072–23080, pMID: 28653822. arXiv:https://doi.org/10.1021/acsami.7b00538, doi:10.1021/acsami.7b00538.
URL https://doi.org/10.1021/acsami.7b00538

[62] K. M. Price, S. Najmaei, C. E. Ekuma, R. A. Burke, M. Dubey, A. D. Franklin, Plasma-enhanced atomic layer deposition of HfO_2 on monolayer, bilayer, and trilayer MoS_2 for the integration of high-κ dielectrics in two-dimensional devices, ACS Applied Nano Materials 2 (7) (2019) 4085–4094. arXiv:https://doi.org/10.1021/acsanm.9b00505, doi:10.1021/acsanm.9b00505.
URL https://doi.org/10.1021/acsanm.9b00505

[63] J. Xu, M. Wen, X. Zhao, L. Liu, X. Song, P.-T. Lai, W.-M. Tang, Effects of HfO_2 encapsulation on electrical performances of few-layered MoS_2 transistor with ALD HfO_2 as back-gate dielectric, Nanotechnology 29 (34) (2018) 345201. doi:10.1088/1361-6528/aac853.
URL https://dx.doi.org/10.1088/1361-6528/aac853

[64] P. Zhao, A. Azcatl, P. Bolshakov, J. Moon, C. L. Hinkle, P. K. Hurley, R. M. Wallace, C. D. Young, Effects of annealing on top-gated MoS_2 transistors with HfO_2 dielectric, Journal of Vacuum Science & Technology B 35 (1) (2017) 01A118. arXiv:https://doi.org/10.1116/1.4974220, doi:10.1116/1.4974220.
URL https://doi.org/10.1116/1.4974220

[65] T. Nam, S. Seo, H. Kim, Atomic layer deposition of a uniform thin film on two-dimensional transition metal dichalcogenides, Journal of Vacuum Science & Technology A 38 (3) (2020) 030803. arXiv:https://doi.org/10.1116/6.0000068, doi:10.1116/6.0000068.
URL https://doi.org/10.1116/6.0000068

[66] V. M. Bermudez, Theoretical study of the adsorption of lewis acids on MoS_2 in relation to atomic layer deposition of Al_2O_3, Journal of Vacuum Science & Technology A 38 (6) (2020) 062412. arXiv:https://doi.org/10.1116/6.0000467, doi:10.1116/6.0000467.
URL https://doi.org/10.1116/6.0000467

[67] P. Giannozzi, S. Baroni, N. Bonini, M. Calandra, R. Car, C. Cavazzoni, D. Ceresoli, G. L. Chiarotti, M. Cococcioni, I. Dabo, A. D. Corso, S. de Gironcoli, S. Fabris, G. Fratesi, R. Gebauer, U. Gerstmann, C. Gougoussis, A. Kokalj, M. Lazzeri, L. Martin-Samos, N. Marzari, F. Mauri, R. Mazzarello, S. Paolini, A. Pasquarello, L. Paulatto, C. Sbraccia, S. Scandolo, G. Sclauzero, A. P. Seitsonen, A. Smogunov, P. Umari, R. M. Wentzcovitch, QUANTUM ESPRESSO: a modular and open-source software project for quantum simulations of materials, Journal of Physics: Condensed Matter 21 (39) (2009) 395502. doi:10.1088/0953-8984/21/39/395502.
URL https://doi.org/10.1088%2F0953-8984%2F21%2F39%2F395502

[68] P. Giannozzi, O. Andreussi, T. Brumme, O. Bunau, M. B. Nardelli, M. Calandra, R. Car, C. Cavazzoni, D. Ceresoli, M. Cococcioni, N. Colonna, I. Carnimeo, A. D. Corso, S. de Gironcoli, P. Delugas, R. A. D. Jr, A. Ferretti, A. Floris, G. Fratesi, G. Fugallo, R. Gebauer, U. Gerstmann, F. Giustino, T. Gorni, J. Jia, M. Kawamura, H.-Y. Ko, A. Kokalj, E. Küçükbenli, M. Lazzeri, M. Marsili, N. Marzari, F. Mauri, N. L. Nguyen, H.-V. Nguyen, A. O. de-la Roza, L. Paulatto, S. Poncé, D. Rocca, R. Sabatini, B. Santra, M. Schlipf, A. P. Seitsonen, A. Smogunov, I. Timrov, T. Thonhauser, P. Umari, N. Vast, X. Wu, S. Baroni, Advanced capabilities for materials modelling with QUANTUM ESPRESSO, Journal of Physics: Condensed Matter 29 (46) (2017) 465901.
URL http://stacks.iop.org/0953-8984/29/i=46/a=465901

[69] P. Giannozzi, O. Baseggio, P. Bonfà, D. Brunato, R. Car, I. Carnimeo, C. Cavazzoni, S. de Gironcoli, P. Delugas, F. Ferrari Ruffino, A. Ferretti, N. Marzari, I. Timrov, A. Urru, S. Baroni, QUANTUM ESPRESSO toward the exascale, The Journal of Chemical Physics 152 (15) (2020) 154105. arXiv:https://doi.org/10.1063/5.0005082, doi:10.1063/5.0005082.
URL https://doi.org/10.1063/5.0005082

[70] L. Bengtsson, Dipole correction for surface supercell calculations, Phys. Rev. B 59 (1999) 12301–12304. doi:10.1103/PhysRevB.59.12301.
URL https://link.aps.org/doi/10.1103/PhysRevB.59.12301

[71] J. P. Perdew, K. Burke, M. Ernzerhof, Generalized gradient approximation made simple, Phys. Rev. Lett. 77 (1996) 3865–3868. doi:10.1103/PhysRevLett.77.3865.
URL https://link.aps.org/doi/10.1103/PhysRevLett.77.3865

[72] J. P. Perdew, A. Ruzsinszky, G. I. Csonka, O. A. Vydrov, G. E. Scuseria, L. A. Constantin, X. Zhou, K. Burke, Restoring the density-gradient expansion for exchange in solids and surfaces, Phys. Rev. Lett. 100 (2008) 136406. doi:10.1103/PhysRevLett.100.136406.
URL https://link.aps.org/doi/10.1103/PhysRevLett.100.136406

[73] S. Grimme, Semiempirical GGA-type density functional constructed with a long-range dispersion correction, Journal of Computational Chemistry 27 (15) (2006) 1787–1799. arXiv:https://onlinelibrary.wiley.com/doi/pdf/10.1002/jcc.20495, doi:10.1002/jcc.20495.
URL https://onlinelibrary.wiley.com/doi/abs/10.1002/jcc.20495

[74] S. Grimme, J. Antony, S. Ehrlich, H. Krieg, A consistent and accurate ab initio parametrization of density functional dispersion correction (DFT-D) for the 94 elements H-Pu, The Journal of Chemical Physics 132 (15) (2010) 154104. arXiv:https://doi.org/10.1063/1.3382344, doi:10.1063/1.3382344.
URL https://doi.org/10.1063/1.3382344

[75] B. G. Janesko, Using nonempirical semilocal density functionals and empirical dispersion corrections to model dative bonding in substituted boranes, Journal of Chemical Theory and Computation 6 (6) (2010) 1825–1833, pMID: 26615842. arXiv:https://doi.org/10.1021/ct1000846, doi:10.1021/ct1000846.
URL https://doi.org/10.1021/ct1000846

[76] H. J. Monkhorst, J. D. Pack, Special points for brillouin-zone integrations, Phys. Rev. B 13 (1976) 5188–5192. doi:10.1103/PhysRevB.13.5188.
URL https://link.aps.org/doi/10.1103/PhysRevB.13.5188

[77] A. Kokalj, XCrySDen–a new program for displaying crystalline structures and electron densities, Journal of Molecular Graphics and Modelling 17 (3) (1999) 176 – 179. doi:https://doi.org/10.1016/S1093-3263(99)00028-5.
URL http://www.sciencedirect.com/science/article/pii/S1093326399000285

[78] Y. Linghu, C. Wu, Gas molecules on defective and nonmetal-doped MoS_2 monolayers, The Journal of Physical Chemistry C 124 (2) (2020) 1511–1522. arXiv:https://doi.org/10.1021/acs.jpcc.9b10450, doi:10.1021/acs.jpcc.9b10450.
URL https://doi.org/10.1021/acs.jpcc.9b10450

[79] V. M. Bermudez, Computational study of the adsorption of NO_2 on monolayer MoS_2, The Journal of Physical Chemistry C 124 (28) (2020) 15275–15284. arXiv:https://doi.org/10.1021/acs.jpcc.0c03786, doi:10.1021/acs.jpcc.0c03786.
URL https://doi.org/10.1021/acs.jpcc.0c03786

[80] M. Sahoo, J. Wang, Y. Zhang, T. Shimada, T. Kitamura, Modulation of gas adsorption and magnetic properties of monolayer-MoS_2 by antisite defect and strain, The Journal of Physical Chemistry C 120 (26) (2016) 14113–14121. arXiv:https://doi.org/10.1021/acs.jpcc.6b03284, doi:10.1021/acs.jpcc.6b03284.

URL https://doi.org/10.1021/acs.jpcc.6b03284

[81] M. Ishii, S. Iwai, H. Kawata, T. Ueki, Y. Aoyagi, Atomic layer epitaxy of AlP and its application to X-ray multilayer mirror, Journal of Crystal Growth 180 (1) (1997) 15–21. doi:https://doi.org/10.1016/S0022-0248(97)00198-X.
URL https://www.sciencedirect.com/science/article/pii/S002202489700198X

[82] M. Ishii, S. Iwai, T. Ueki, Y. Aoyagi, Observation and control of surface morphology of AlP grown by atomic layer epitaxy, Applied Physics Letters 71 (8) (1997) 1044–1046. arXiv:https://doi.org/10.1063/1.119722, doi:10.1063/1.119722.
URL https://doi.org/10.1063/1.119722

[83] S. A. Trifonov, V. A. Lapikov, A. A. Malygin, Reactivity of phenol-formaldehyde microspheres toward PCl_3, $VOCl_3$, and CrO_2Cl_2 vapors, Russian Journal of Applied Chemistry 75 (6) (2002) 969–973. doi:10.1023/A:1020301216385.
URL https://doi.org/10.1023/A:1020301216385

[84] Y. D. Kim, M. S. Lee, T.-W. Lee, H. Hwang, S. Yoon, Y. Moon, E. Yoon, In situ analysis of surface photoabsorption spectra during InP ALE in metal organic chemical vapor deposition, Microelectronic Engineering 51-52 (2000) 43–50. doi:https://doi.org/10.1016/S0167-9317(99)00459-1.
URL https://www.sciencedirect.com/science/article/pii/S0167931799004591

[85] M. Ozeki, T. Haraguchi, T. Takeuchi, K. Maeda, A comparative study of the growth mechanism of InAs/GaAs and GaP/GaAs heterostructures and strained layered superlattices by atomic layer epitaxy, Journal of Crystal Growth 276 (3) (2005) 374–380. doi:https://doi.org/10.1016/j.jcrysgro.2004.11.427.
URL https://www.sciencedirect.com/science/article/pii/S0022024804019190

[86] M. J. Szary, MoS_2 doping for enhanced H_2S detection, Applied Surface Science 547 (2021) 149026. doi:https://doi.org/10.1016/j.apsusc.2021.149026.
URL https://www.sciencedirect.com/science/article/pii/S0169433221001021